FINITE ELEMENT SIMULATION OF LARGE RAM-AIR PARACHUTES

S. Mittal
Department of Aerospace Engineering
Indian Institute of Technology
Kanpur, UP 208 016

and

T. Tezduyar
Army HPC Research Center
University of Minnesota
Minneapolis, MN 55415, USA

Abstract

Ram air parachutes have been fairly popular with the sports community owing to their high efficiency and control. In the past few years, defence organizations throughout the world have been considering, quite seriously, of deploying these parafoils in their operations. In the near future, large ram-air parachutes are expected to provide the capability of delivering 21-ton payloads from altitudes as high as 25,000 ft. Compared to the drop tests, to evaluate the performance of these parachutes in the developmental stage, the numerical simulations provide a much cheaper alternative. In this direction, efforts have been made to model the dynamics of ram-air parachutes using advanced finite-element techniques. Two sets of numerical studies are conducted. The first one involves the simulation of the steady gliding flight of the parafoil at the desired configuration. Results of the simulations are compared with the wind tunnel data available from previous experimental studies. In the second set of simulations, the efforts are directed to study the dynamics of the parachute during the inflation stage. In the early stages of the canopy inflation the parachute is modeled as an expanding box, whereas at the later stages the box transforms to a parafoil as it expands and glides. Time histories of the forces acting on the parafoil in the expansion process are also recorded.

1 Introduction

Ram-air parachutes are quite commonly used by the sports parachute community. Compared to the, conventional, circular-canopy parachutes these ram-air parachutes offer significantly higher controllability and efficiency. Military organizations also utilize them to drop personnel, stores and light payloads with high reliability and accuracy. Larger version of these parachutes are being designed that will provide the capability of delivering 21 ton payloads from altitudes as high as 25,000 ft with increased accuracy and reduced impact. Such parachutes will be an order of magnitude larger and will have a wing-loading three times larger than the existing ones.

The design of such large parachute systems involves a series of challenging problems [1, 2, 3]. During the inflation stage, one would like to have a reasonable estimate of the opening forces so that a suitable material can be chosen. The inflation of a parachute is a complex process involving turbulent flow over rapidly deforming, porous membranes and an interaction between the parachute structure and payload. The stability of the canopy and its interaction with the cables in the inflation stage is another issue that plays a vital role in the design of the parachute.

In this article we present finite element flow simulation techniques to model the various stages of flight of parachute systems. In one of the studies, the performance of the ram air parachute in a steady gliding flight is computed. Later, the methodology is used to model the inflation stage of the parachute from a box-like configuration to a full blown parafoil. The air flow around the canopy is governed by the incompressible, 3D Navier-Stokes equations. The dynamics of the canopy is governed by the Newton's law of motion. The forces acting on the canopy are calculated from the simulated flow field. At the initial stage of canopy inflation the parachute is modeled as a falling expanding box, whereas at the later stages, the box transforms to an expanding, gliding parafoil. To handle the inflation of the canopy in solving the fluid-flow equations, we employ the Deformable-Spatial-Domain/Stabilized-Space-time (DSD/SST) finite element formulation [4, 5]. All the computations reported in this article are carried out at the Army High Performance Computing Research Center on the Thinking Machines CM-5 massively parallel computer [6].

2 The Governing Equations

Let $\Omega \subset R^{n_{sd}}$ and $(0,T)$ be the spatial and temporal domains respectively, where n_{sd} is the number of space dimensions, and let Γ denote the boundary of Ω. The spatial and temporal coordinates are denoted by $\mathbf{x}$ and t. The Navier-Stokes equations governing incompressible fluid flow are

$$\rho(\frac{\partial \mathbf{u}}{\partial t} + \mathbf{u}\cdot\nabla\mathbf{u} - \mathbf{f}) - \nabla\cdot\boldsymbol{\sigma} = \mathbf{0} \qquad \text{on } \Omega \text{ for } (0,T) \quad (1)$$

$$\nabla\cdot\mathbf{u} = 0 \qquad \text{on } \Omega \text{ for } (0,T) \quad (2)$$

Here ρ, $\mathbf{u}$, $\mathbf{f}$ and $\boldsymbol{\sigma}$ are the density, velocity, body force and the stress tensor, respectively. The stress tensor is written as the sum of its isotropic and deviatoric parts:

$$\boldsymbol{\sigma} = -p\mathbf{I} + \mathbf{T}, \quad \mathbf{T} = 2\mu\boldsymbol{\varepsilon}(\mathbf{u}),$$
$$\boldsymbol{\varepsilon}(\mathbf{u}) = \frac{1}{2}((\nabla\mathbf{u}) + (\nabla\mathbf{u})^T), \quad (3)$$

where p and μ are the pressure and viscosity. Both the Dirichlet and Neumann-type boundary conditions are accounted for, represented as

$$\mathbf{u} = \mathbf{g} \text{ on } \Gamma_g, \quad \mathbf{n}\cdot\boldsymbol{\sigma} = \mathbf{h} \text{ on } \Gamma_h, \quad (4)$$

where Γ_g and Γ_h are complementary subsets of the boundary Γ. The initial condition on the velocity is specified on Ω:

$$\mathbf{u}(\mathbf{x},0) = \mathbf{u}_0 \quad \text{on } \Omega, \quad (5)$$

where $\mathbf{u}_0$ is divergence free.

3 Finite Element Formulation

Consider a finite element discretization of Ω into subdomains Ω^e, $e = 1,2,...,n_{el}$, where n_{el} is the number of elements. Based on this discretization, for velocity and pressure we define the finite element trial function spaces $\mathcal{S}_{\mathbf{u}}^h$ and $\mathcal{S}_p^h$, and weighting function spaces $\mathcal{V}_{\mathbf{u}}^h$ and $\mathcal{V}_p^h$. These function spaces are selected, by taking the Dirichlet boundary conditions into account, as subsets of $[\mathbf{H}^{1h}(\Omega)]^{n_{sd}}$ and $\mathbf{H}^{1h}(\Omega)$, where $\mathbf{H}^{1h}(\Omega)$ is the finite-dimensional function space over Ω. The stabilized finite element formulation of Eq. (1)-(2) is written as follows: find $\mathbf{u}^h \in \mathcal{S}_{\mathbf{u}}^h$ and $p^h \in \mathcal{S}_p^h$ such that $\forall \mathbf{w}^h \in \mathcal{V}_{\mathbf{u}}^h$, $q^h \in \mathcal{V}_p^h$

$$\int_\Omega \mathbf{w}^h\cdot\rho\left(\frac{\partial\mathbf{u}^h}{\partial t} + \mathbf{u}^h\cdot\nabla\mathbf{u}^h - \mathbf{f}\right)d\Omega + \int_\Omega \boldsymbol{\varepsilon}(\mathbf{w}^h) : \boldsymbol{\sigma}(p^h,\mathbf{u}^h)d\Omega + \int_\Omega q^h\nabla\cdot\mathbf{u}^h d\Omega + \sum_{e=1}^{n_{el}}\int_{\Omega^e}\frac{1}{\rho}\left(\tau_{\text{SUPG}}\rho\mathbf{u}^h\cdot\nabla\mathbf{w}^h + \tau_{\text{PSPG}}\nabla q^h\right)\cdot \left[\rho\left(\frac{\partial\mathbf{u}^h}{\partial t} + \mathbf{u}^h\cdot\nabla\mathbf{u}^h - \mathbf{f}\right)\right] + \sum_{e=1}^{n_{el}}\int_{\Omega^e}\delta\nabla\cdot\mathbf{w}^h\rho\nabla\cdot\mathbf{u}^h d\Omega^e = \int_{\Gamma_h}\mathbf{w}^h\cdot\mathbf{h}^h d\Gamma \quad (6)$$

Remarks

1. In the variational formulation given by Eq. (6), the first three terms and the right-hand-side constitute the Galerkin formulation of the problem.

2. The first series of element-level integrals are the SUPG and PSPG stabilization terms added to the variational formulations [7, 8]. In the current formulation τ_{PSPG} is the same as τ_{SUPG} and is given as

$$\tau = \left(\left(\frac{2\parallel\mathbf{u}^h\parallel}{h}\right)^2 + \left(\frac{4\nu}{h^2}\right)^2\right)^{-\frac{1}{2}} \quad (7)$$

3. The second series of element-level integrals are added to the formulation for numerical stability at high Reynolds numbers. This is a least-squares term based on the continuity equation. The coefficient δ is defined as

$$\delta = \frac{h}{2}\parallel\mathbf{u}^h\parallel z, \quad (8)$$

where

$$z = \begin{cases} \left(\frac{Re_u}{3}\right) & Re_u \le 3 \\ 1 & Re_u > 3 \end{cases}, \quad (9)$$

and Re_u is the cell Reynolds number.

4. Both stabilization terms are weighted residuals, and therefore maintain the consistency of the formulation.

4 Numerical Simulations

All the computations reported in this article are carried using equal-in-order trilinear basis functions for velocity and pressure. The non-linear equation systems resulting from the finite-element discretization of the flow equations are solved using a matrix-free implementation of the Generalized Minimal RESidual (*GMRES*) technique [9] in conjunction with diagonal preconditioners.

4.1 Steady-state glide at Re 10^7

The cross-section of the parafoil is a Clark-Y airfoil with a rounded leading edge. The aspect ratio is 3.0 and ratio of line-length to span is 0.6. The finite element mesh consists of 291,437 nodes and 279,888 hexahedral elements. No-slip condition is imposed on the parafoil surface; zero-shear stress and zero-normal velocities at the side boundaries, velocity at the inflow boundary and traction free conditions at the outflow

boundary are specified. At every time-step 1,129,248 nonlinear equations are solved. A simplified version of the algebraic Baldwin-Lomax [10] turbulence model is incorporated:

$$\mu_t = \rho l^2 |\omega|, \quad (10)$$

$$l = \kappa n(1 - exp(-n^+/A^+)), \quad (11)$$

where μ_t is the eddy viscosity, ω is the vorticity vector, $\kappa = 0.41$ and $A^+ = 25.0$ are constants, n is the wall distance to the wall, and n^+ is the same distance in wall units. In the present computations, this distance is measured from the closest node on the surface. The x-axis is along the chord while the y-axis is along the span of the parafoil; c is the chordlength while b denotes the span of the parafoil.

Figure 1 shows the chordwise pressure distribution on the parafoil surface at midspan ($y/b = 0$) for various angles of attack. The chordwise pressure distribution, close to the tip of the parafoil ($y/b = 0.45$) are shown in Figure 2. We observe that the pressure distribution at the midspan is quite similar to that for a 2D airfoil, while the 3D effects are quite significant close to the tip and lead to a net loss of lift. The 3D effects are due to the leakage of leakage of fluid around the tips from the lower to upper surface. Figures 3, 4 and 5 show the spanwise distribution of pressure on the parafoil at various chordwise locations for several angles of attack. The pressure (load) distribution is almost elliptic with the effect of cells quite significant close to the leading edge. However, it should be pointed out that this might be an artifact of our modeling the parafoil as a closed section, without a cut at the leading edge. In a real flight, the leading edge of the parafoil traps a stagnant vortex that results in a flatter pressure distribution.

Figure 6 shows the variation of the lift and drag coefficients with angle of attack. A factor of $0.5h/c$ is added to the drag coefficient to account for the inlet [11], where, h is the inlet height. Here, $h/c = 0.1$ is used. The variation of the lift to drag ratio is shown in Figure 7. Compared to the experimental data, our results overpredict the L/D value. This can be attributed to several reasons. Our results do not account for the line and payload drag. Close to the stall angle, the flow starts separating from the parafoil surface. It is well known that the current turbulence model is not valid in flows with recirculating regions. Additionally, the effect of a cut at the leading edge of the parafoil is not very well known.

Figures 8 and 9 show the pressure distribution on the parafoil surface obtained with two different meshes. We observe a good agreement between the two solutions and this establishes the convergence of the solution with respect to the meshes. Figure 10 shows the pressure distribution on the surface of the parafoil for one of the cases.

4.2 Simulation of inflation dynamics

The inflation of a ram-air inflated gliding parachute takes place in three stages [12]. In the first stage, the canopy expands with little cell inflation. The canopy then pitches forward to and inflates because of the air that rushes into the separate cells of the gliding wing. This causes the canopy to take form resulting in a loss of drag and generation of lift. The parachute then transitions to equilibrium glide.

In these computations, the parafoil falls under gravity, inflates and settles to a steady gliding angle. The pitching motion of the canopy is not accounted for in the present simulation. A partially inflated box of dimensions $48.0 \times 33.4 \times 12.0$ ft^3 (*chord* $\times$ *span* $\times$ *thickness*) transforms to a gliding parafoil at a prescribed rate. The box expands by factors of 1.5 in the chordwise and 6.5 in the spanwise directions. The cross-section transforms from a rectangular one to a NACA 0025 section. Figure 11 shows the surface mesh of the parachute during this transformation.

The finite element mesh consists of 170,950 nodes and 161,856 hexahedral elements. This results in a nonlinear equation system of 1,304,606 equations that have to be solved at each time step.

At $t = 0.0$ s the computations begin with an initial condition corresponding to the steady-state past a box at 10^o angle of attack and a velocity of 112 ft/s. At $t = 2.0$ s the box transforms completely to a parafoil but the computations continue till $t = 3.5$ s. The parafoil/payload system weight is 22,000 *lbs*.

Figures 12 and 13 show the time histories of the projection area and the velocity of the parafoil, respectively. Initially, the box generates very little lift and accelerates under the action of gravity. As it expands rapidly, very large aerodynamic forces are generated as shown in Figure 14. At the end, the parafoil attains an almost steady gliding angle of attack of approximately 4^o as shown in Figure 15.

5 Conclusions

A very powerful tool for investigating the performance of the ram-air parafoils has been developed. It has been applied to study the steady-state gliding performance and also the inflation dynamics of such parachute systems. Reasonable comparisons are observed between the computed solutions and the wind tunnel and drop tests.

References

[1] J.S. Lingard. Unsteady aerodynamics. In *University of Minnesota Parachute Systems Technology Short Course*, League City, TX, 1994.

[2] S.K. Aliabadi, W.L. Garrard, V. Kalro, S. Mittal, T.E. Tezduyar, and K.R. Stein. Parallel finite element computations of the dynamics of large

ram air parachutes. In *AIAA Paper 95-1581, 13th Aerodynamic Decelerator and Systems Conference*, pages 278–293, Clearwater, Fl, 1995.

[3] W.L. Garrard, T.E. Tezduyar, S.K. Aliabadi, V. Kalro, J. Luker, and S. Mittal. Inflation analysis ram air inflated gliding parachutes. In *AIAA Paper 95-1565, 13th Aerodynamic Decelerator and Systems Conference*, pages 186–198, Clearwater, Fl, 1995.

[4] T.E. Tezduyar, M. Behr, and J. Liou. A new strategy for finite element computations involving moving boundaries and interfaces – the deforming-spatial-domain/space-time procedure: I. The concept and the preliminary tests. *Computer Methods in Applied Mechanics and Engineering*, 94(3):339–351, 1992.

[5] T.E. Tezduyar, M. Behr, S. Mittal, and J. Liou. A new strategy for finite element computations involving moving boundaries and interfaces – the deforming-spatial-domain/space-time procedure: II. Computation of free-surface flows, two-liquid flows, and flows with drifting cylinders. *Computer Methods in Applied Mechanics and Engineering*, 94(3):353–371, 1992.

[6] M. Behr, A. Johnson, J. Kennedy, S. Mittal, and T.E. Tezduyar. Computation of incompressible flows with implicit finite element implementations on the Connection Machine. *Computer Methods in Applied Mechanics and Engineering*, 108:99–118, 1993.

[7] T.E. Tezduyar, S. Mittal, S.E. Ray, and R. Shih. Incompressible flow computations with stabilized bilinear and linear equal-order-interpolation velocity-pressure elements. *Computer Methods in Applied Mechanics and Engineering*, 95:221–242, 1992.

[8] S. Mittal. *Stabilized Space-Time Finite Element Formulations for Unsteady Incompressible Flows Involving Fluid-Body Interactions.* PhD thesis, University of Minnesota, 1992.

[9] Y. Saad and M. Schultz. GMRES: A generalized minimal residual algorithm for solving nonsymmetric linear systems. *SIAM Journal of Scientific and Statistical Computing*, 7:856–869, 1986.

[10] B. Baldwin and H. Lomax. Thin layer approximation and algebaric turbulence model for separated turbulent flows. In *AIAA Paper 78-257, AIAA 16th Aerospace Sciences Meeting*, Huntsville, Alabama, 1978.

[11] J.S. Lingard. Ram-air parachute design. In *13th Aerodynamic Decelerator Conference, 2nd ADS Technolgy Seminar*, Clearwater, Florida, 1995.

[12] J.S. Lingard. A semi-empirical theory to predict the load-time history of an inflating parachute. In *AIAA Paper 84-0814, 8th Aerodynamic Decelerator and Balloon Technology Conference*, pages 177–185, Hyannis, MA, 1984.

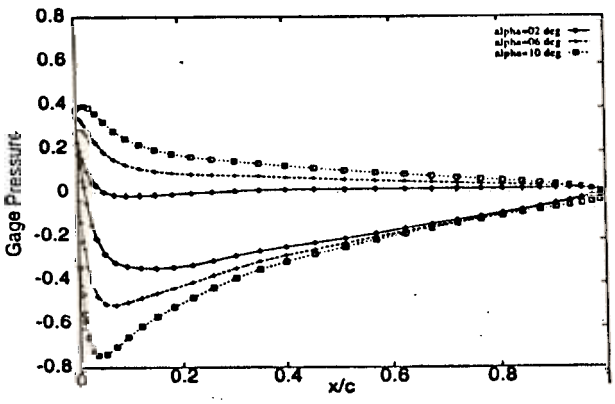

Figure 1. Steady-state simulations at $Re = 10^7$ for various angles of attack: chord-wise pressure distribution on the paral surface at y/b=0.00 (midspan).

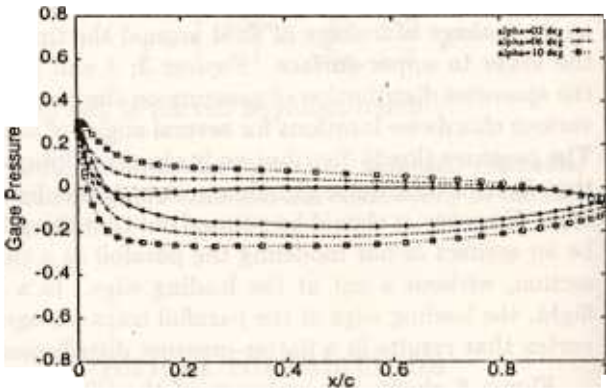

Figure 2. Steady-state simulations at $Re = 10^7$ for various angles of attack: chord-wise pressure distribution on the pan surface at y/b=0.45.

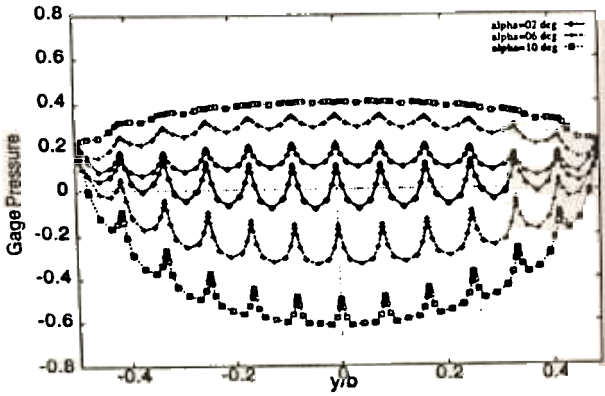

Figure 3. Steady-state simulations at $Re = 10^7$ for various angles of attack: span-wise pressure distribution on the paral surface at x/c=0.02.

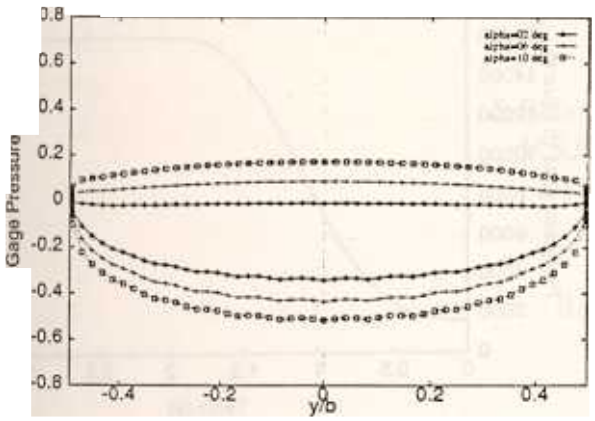

Figure 4. Steady-state simulations at $Re = 10^7$ for various angles of attack: span-wise pressure distribution on the parafoil surface at x/c=0.25.

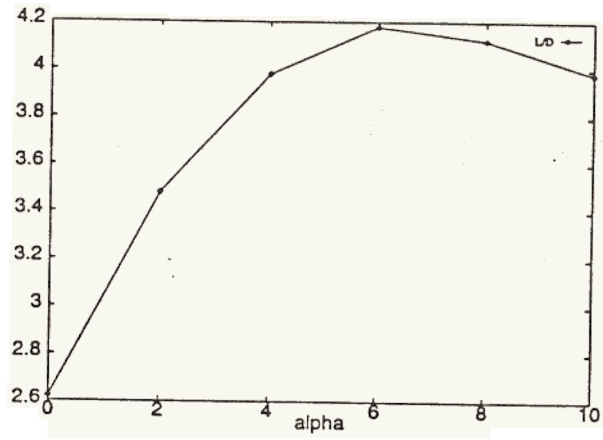

Figure 7. Steady-state simulations at $Re = 10^7$: lift/drag (L/D) ratio as function of angle of attack.

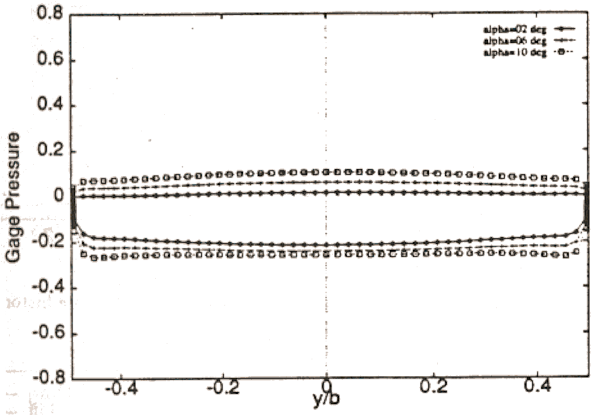

Figure 5. Steady-state simulations at $Re = 10^7$ for various angles of attack: span-wise pressure distribution on the parafoil surface at x/c=0.50.

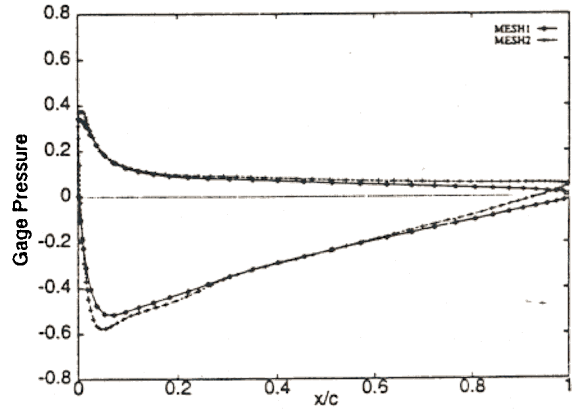

Figure 8. Steady-state simulations at $Re = 10^7$, at $\alpha = 6°$: chord-wise pressure distribution on the parafoil surface at y/b=0.00. Comparison of the solutions on Mesh 1 (291.437 nodes) and Mesh 2 (594.587 nodes).

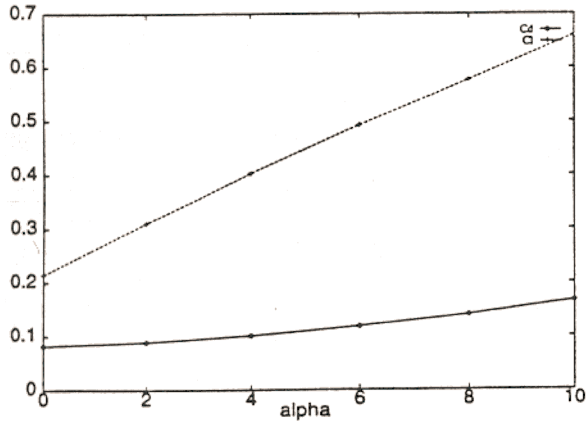

Figure 6. Steady-state simulations at $Re = 10^7$: drag and lift coefficients as functions of angle of attack.

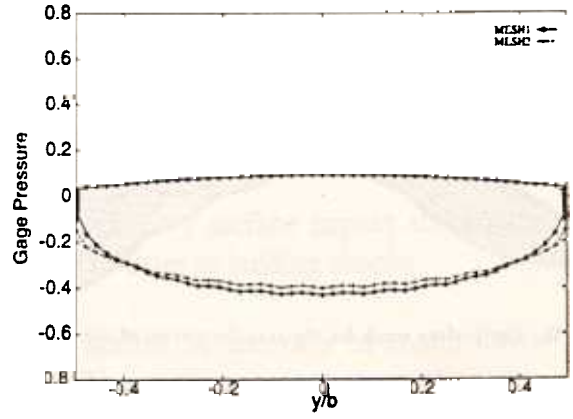

Figure 9. Steady-state simulations at $Re = 10^7$, at $\alpha = 6°$: span-wise pressure distribution on the parafoil surface at x/c=0.25. Comparison of the solutions on Mesh 1 (291.437 nodes) and Mesh 2 (594.587 nodes).

Figure 10. Steady-state simulations at $Re = 10^7$, at $\alpha = 2°$: pressure distribution on parafoil surface.

Figure 11. The surface mesh for the transformation of the box to a parafoil.

Figure 15. Transformation of the box to a parafoil: time history of the angle of attack.

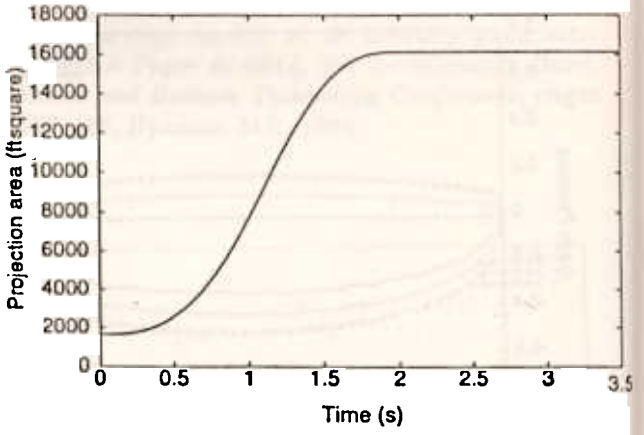

Figure 12. Transformation of the box to a parafoil: time history of the projection area.

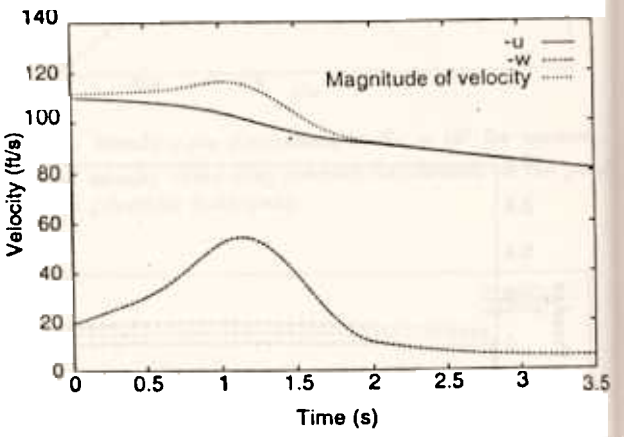

Figure 13. Transformation of the box to a parafoil: time history of the parafoil velocity.

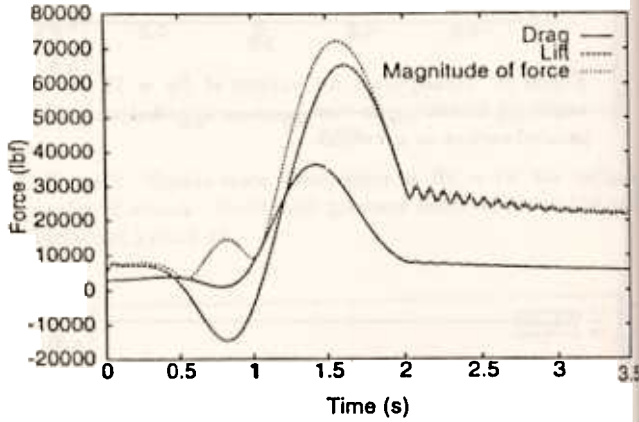

Figure 14. Transformation of the box to a parafoil: time history of the forces acting on the parafoil.